Nuclear Science and Techniques (2026) 37:49
https://doi.org/10.1007/s41365-025-01861-7

Improving MCUCN code to simulate ultracold neutron storage and transportation in superfluid ^{4}He

Xue-Fen Han[1,2,3] · **Fei Shen**[1,2] · **Bin Zhou**[1,2] · **Xiao-Xiao Cai**[1,2] · **Tian-Cheng Yi**[1,2] · **Zhi-Liang Hu**[1,2] · **Song-Lin Wang**[1,2] · **Tian-Jiao Liang**[1,2,3,4] · **Robert Golub**[5]

Received: 16 May 2024 / Revised: 16 July 2024 / Accepted: 9 September 2024 / Published online: 10 January 2026
© The Author(s), under exclusive licence to China Science Publishing & Media Ltd. (Science Press), Shanghai Institute of Applied Physics, the Chinese Academy of Sciences, Chinese Nuclear Society 2026

Abstract

The ultracold neutron (UCN) transport code, MCUCN, designed initially for simulating UCN transportation from a solid deuterium (SD_2) source and neutron electric dipole moment experiments, could not simulate UCN storage and transportation in a superfluid ^{4}He (SFHe, He-II) source accurately. This limitation arose from the absence of an ^{4}He upscattering mechanism and the absorption of ^{3}He. And the provided source energy distribution in MCUCN is different from that in SFHe source. This study introduced enhancements to MCUCN to address these constraints, explicitly incorporating the ^{4}He upscattering effect, the absorption of ^{3}He, the loss caused by impurities on converter wall, UCN source energy distribution in SFHe, and the transmission through negative optical potential. Additionally, a Python-based visualization code for intermediate states and results was developed. To validate these enhancements, we systematically compared the simulation results of the Lujan Center Mark3 UCN system by MCUCN and the improved MCUCN code (iMCUCN) with UCNtransport simulations. Additionally, we compared the results of the SUN1 system simulated by MCUCN and iMCUCN with measurement results. The study demonstrates that iMCUCN effectively simulates the storage and transportation of ultracold neutrons in He-II.

Keywords Ultracold neutron · Storage · Transportation · Improved MCUCN code · Upscattering effect · Absorption by ^{3}He

1 Introduction

Ultracold neutrons possess kinetic energy less than 300 neV, equivalent to temperatures below 3 mK or wavelengths longer than 500 Å [1]. Their low energy allows complete reflection and confinement in materials with high Fermi potential [2, 3], facilitating easy storage and counting. Since their discovery in 1969 [4, 5], UCNs have been pivotal in studying fundamental physics, encompassing the measurement of neutron electric dipole moment [6], neutron lifetime [7], beta decay [8, 9], gravitational resonance spectroscopy [10, 11], neutrino asymmetry [12], neutron–antineutron oscillations [13], and surface characterization of materials [14]. These experiments hold promise for investigating CP-violating mechanisms beyond the standard model, the origin of the baryon asymmetry in the universe [15], the neutron lifetime puzzle, the key parameter in the Big Bang theory, the real neutron loss mechanism, the fifth force, dark matter, and so on.

SFHe and SD_2 are superthermal materials for producing UCNs through neutron inelastic scattering. The neutron

---

This work was supported by the National Key R&D Program of China (No. 2024YFE0110001), the National Natural Science Foundation of China (U1932219), and the Mobility Programme endorsed by the Joint Committee of the Sino-German Center (M-0728).

✉ Tian-Jiao Liang
liangtj@ihep.ac.cn

[1] Institute of High Energy Physics, Chinese Academy of Sciences (CAS), Beijing 100049, China

[2] Spallation Neutron Source Science Center (SNSSC), Dongguan 523803, China

[3] University of Chinese Academy of Sciences, Beijing 100049, China

[4] Guangdong-Hong Kong-Macao Joint Laboratory for Neutron Scattering Science and Technology, Dongguan 523803, Guangdong, China

[5] Department of Physics, North Carolina State University, Raleigh 27695, USA

absorption on deuteron limits the UCN lifetime in SD_2, necessitating a UCN buffer volume for storage. Conversely, UCNs can be stored in SFHe until they decay due to zero absorption cross section, making SFHe converters viable as experimental bottles [16]. Additionally, the ideal UCN density in SFHe can be significantly higher than in SD_2 [17]. While SD_2 UCN sources have seen substantial development over the last 40 years [18–25] and recognized as leading UCN sources globally [26, 27], SFHe UCN sources are gaining prominence, with the CSNS [28–32] team presently designing a He-II-based UCN source.

To characterize and optimize UCN storage and transportation processes, Monte Carlo-based UCN codes such as PENTrack [33], GEANT4UCN [34], UCNtransport [35], and MCUCN [36] are available. Despite sharing core physical models, each software has merits, such as PENTrack's flexible geometry configuration interface and GEANT4UCN's including neutron spins, protons, and electron simulations in electromagnetic fields. UCNtransport, while valuable, is not open source. Conversely, MCUCN code offers significant advantages being open source. It is highly extensible and can be executed in parallel via a shell script. However, it suffers from certain limitations when it is used to simulate SFHe UCN source, including the absence of critical models that describe ^{4}He upscattering, ^{3}He absorption, and impurities on converter wall. Furthermore, it lacks the capability to represent the source energy distribution for SFHe and simulate UCN transmission through materials with a negative optical potential.

To enhance the MCUCN code, we performed several modifications, including: (1) The incorporation of an ^{4}He upscattering physical model. (2) The inclusion of a ^{3}He absorption model. (3) The introduction of an impurities model. (4) Improvements to the source energy distribution in SFHe and geometric description. (5) The addition of transmission capabilities for materials with negative optical potential. (6) Development of visualization tools for simulating intermediate states and results. Section 2 of this paper outlines the physical models and flow of the iMCUCN code. Section 3 presents the results simulated by MCUCN, iMCUCN, and UCNtransport. Section 4 compares the results of MCUCN and iMCUCN with experimental data. Consequently, iMCUCN is deemed valid and promising for UCN storage and transportation simulations in He-II.

2 Physical model enhancement and flow of iMCUCN

The basic theory and key attributes of the MCUCN are outlined in detail in reference [36]. This code is a tool for Monte Carlo-based ultracold neutron transport simulations, focusing on the intricate interactions between UCNs and materials. However, certain limitations in its current form necessitate enhancements for a more comprehensive representation of UCN behavior in SFHe.

Currently, MCUCN does not account for the upscattering effect of ^{4}He, the absorption of ^{3}He, and the loss due to impurities. Moreover, the code does not consider the UCN source energy distribution in SFHe. Furthermore, the omission of UCN transmission through materials with negative optical potential represents a notable gap, playing a pivotal role in the simulations detailed in Sect. 3. Additionally, MCUCN lacks built-in visualization tools, leaving the task of developing suitable visualization mechanisms to the user. To address these limitations and enable the simulation of UCN storage and transportation in SFHe more accurately, enhancements to MCUCN are imperative.

2.1 The loss mechanisms in SFHe

For He-II, it is possible to formulate the expression for the ultracold neutron surviving time in terms of various loss mechanisms [37–39]:

$$\tau^{-1} = \tau_{\mathrm{up}}^{-1} + \tau_{\mathrm{abs}}^{-1} + \tau_{\mathrm{wall}}^{-1} + \tau_{\beta}^{-1} + \tau_{\mathrm{leakage}}^{-1} + \tau_{\mathrm{impurities}}^{-1}. \tag{1}$$

Here, the reciprocal of τ represents the UCN total loss rate. τ_{up}^{-1} is influenced by the UCN upscattering effect in He-II. τ_{abs}^{-1} arises from the substantial neutron absorption cross section of ^{3}He. When a UCN encounters a wall coated with a material of high Fermi potential, losses may occur due to wall absorption and upscattering ($\tau_{\mathrm{wall}}^{-1}$). The parameter $\tau_{\beta} = 880$ s represents the neutron decay time. $\tau_{\mathrm{leakage}}^{-1}$ is the UCN leakage from gaps of UCN valve and storage volume wall. $\tau_{\mathrm{impuritie}}$ is the loss caused by absorption and up-scattering of impurities which deposit on the walls of the production volume [39]. While MCUCN includes wall collisions, leakage, and decay models, it lacks crucial additional loss mechanisms.

The upscattering rate of superfluid ^{4}He τ_{up} is temperature dependent and can be divided into three parts [40]: one-phonon absorption, two-phonon scattering, and roton–phonon scattering. Yoshiki et al. summarized the formula for τ_{up} [41] as:

$$\frac{1}{\tau_{\mathrm{up}}} = Ae^{\frac{-12}{T}} + BT^{7} + CT^{\frac{3}{2}}e^{-\frac{8.6}{T}}, \tag{2}$$

where the first term originates from one-phonon absorption, the second from two-phonon scattering, and the third from roton–phonon scattering. Thus, the upscattering time constant is related to the He-II temperature. According to measurements in Ref. [42], $A = 61.1\,\mathrm{s}^{-1}$, $B = 7.6 \times 10^{-3}\,\mathrm{s}^{-1}\mathrm{K}^{-7}$, and $C = 5.22\,\mathrm{s}^{-1}\mathrm{K}^{-7}$ for 1.6 K He-II, resulting in $\tau_{\mathrm{up}} = 3.4$ s. For $T = 0.7$ K, $A = 130\,\mathrm{s}^{-1}$ [40, 43], $B = 9.0 \times 10^{-3}\,\mathrm{s}^{-1}\mathrm{K}^{-7}$,

$C = 18\,\mathrm{s}^{-1}\mathrm{K}^{-7}$, leading to $\tau_{\mathrm{up}} = 1247$ s. The UCN upscattering loss rate in He-II has been experimentally confirmed in Refs. [40, 44] and plays a significant role at higher temperatures but a lesser role at lower temperatures.

According to Ref. [38], the wall loss time constant τ_{wall} is defined as:

$$\frac{1}{\tau_{\mathrm{wall}}} = \frac{\bar{\mu}\left(E_{\mathrm{UCN}}\right) v S}{4V}, \tag{3}$$

where $\bar{\mu}\left(E_{\mathrm{UCN}}\right)$ is the average loss probability per bounce, dependent on UCN energy. It is noteworthy that higher energy UCNs are more likely to be lost compared to lower energy ones. Here, V represents the converter volume, S is its surface area, and v denotes the neutron velocity in vacuum.

The absorption time constant τ_{abs} is given by:

$$\frac{1}{\tau_{\mathrm{abs}}} = n_{^3\mathrm{He}}\sigma_{\mathrm{a}} v = n_{^3\mathrm{He}}\sigma_{\mathrm{a}_{(\mathrm{th})}} v_{(\mathrm{th})}. \tag{4}$$

This term remains independent of UCN velocity due to the $1/v$ principle of the ^{3}He thermal neutron absorption cross section σ_{a}. σ_{a} is 5333 b at a velocity of 2200 m/s. The notation $n_{^3\mathrm{He}}$ denotes the number density of ^{3}He atoms. The natural abundance ratio of $n_{^3\mathrm{He}}$ to $n_{^4\mathrm{He}}$, at 1.37×10^{-6}, corresponds to $3 \times 10^{-16}\,\mathrm{cm}^{-3}$ at 1 K and an absorption time constant of 0.028 s. This parameter remains crucial in the total loss rate calculation until the abundance of ^{3}He is reduced to below 10^{-12}.

The leakage time constant τ_{leakage} is defined as:

$$\frac{1}{\tau_{\mathrm{leakage}}} = \frac{S_{\mathrm{leakage}}\, v}{4V}. \tag{5}$$

In comparison with τ_{wall}, this term corresponds to wall loss with $\mu = 1$, where $\mathrm{S}_{\mathrm{leakage}}$ represents the total area of gaps that can leak UCNs.

2.2 Initial energy distribution in SFHe

The MCUCN code incorporates uniform and Gaussian energy distributions but does not include other forms of energy spectrum distribution. To simulate the SFHe UCN source, we integrated a Monte Carlo sampling function to generate the energy distribution that accurately represents the superfluid helium UCN source.

The relationship between the real space UCN density n with energy E in the range $(E, E + \mathrm{d}E)$ and the phase space density ρ is [38]

$$n(E)\mathrm{d}E = \frac{\mathrm{d}^3 N}{\mathrm{d}^3 r} = \rho \mathrm{d}^3 p, \tag{6}$$

where $\mathrm{d}^3 r \mathrm{d}^3 p$ is the phase space volume and $\mathrm{d}^3 r$ is the real space volume. N is the UCN number. When produced in SFHe, the UCNs fill the phase space with a constant density of ρ. Then

$$n(E)\mathrm{d}E \propto p^2 \mathrm{d}p \propto \sqrt{E}\mathrm{d}E. \tag{7}$$

Thus the initial UCN spectrum in SFHe converter is

$$\mathrm{d}P_{\mathrm{source}} \propto \sqrt{E}\mathrm{d}E. \tag{8}$$

2.3 The iMCUCN code

As depicted in Fig. 1, the iMCUCN code models UCN losses during transportation. The red sections delineate mechanisms for (a) generating the energy distribution of the UCN source in SFHe, (b) simulating the upscattering effect of ^{4}He, (c) simulating absorption by residual ^{3}He contamination, (d) simulating absorption and upscattering by impurities, (e) simulating UCN transmission through materials with negative optical potential. Polypropylene (PP) possesses a negative optical potential and serves as the foil confining SFHe [45]. The code MCUCN incorporates transmission physics through materials with positive optical potential but overlooks those with negative potential. Thus it is necessary to integrate the negative potential for PP foil in next section. The iMCUCN code also integrates geometry descriptions to simulate various volumes and includes a visualization component. UCNs are considered lost upon encountering the detector, the heat exchanger, or other components.

Figure 1 showcases the iMCUCN's physical model, symbolized by diamonds [36]. Absorption may result in the loss of UCNs produced in the deuterium converter, yet the absorption rate within the superfluid ^{4}He UCN source is zero. Neutrons undergo continuous decay during simulations, with ^{4}He upscattering effects and ^{3}He absorption occurring solely in He-II. Impurities are identified on the wall of converter. UCNs encountering surfaces of the detector, heat exchanger, and other components are either lost or detected. Upon collision with a wall surface, UCNs will pass through if the wall is virtual, or they may be reflected, absorbed, or transmitted through the surface. Reflections manifest as either diffuse or specular, allowing reflected UCNs to persist and embark on subsequent collision. Surface absorption arises from both absorption and inelastic scattering by the wall. The simulation concludes for a UCN upon reaching the exit window, i.e., the detector, marking the end of its journey and prompting the initiation of a new cycle with the generation of another UCN in the converter.

Fig. 1 Illustration of the flow of physical models in the iMCUCN code [36]. Diamonds indicate the physical models utilized for selecting a loss mechanism or going to exit window during transportation. Black characters represent original code sections, whereas our additions are highlighted in red

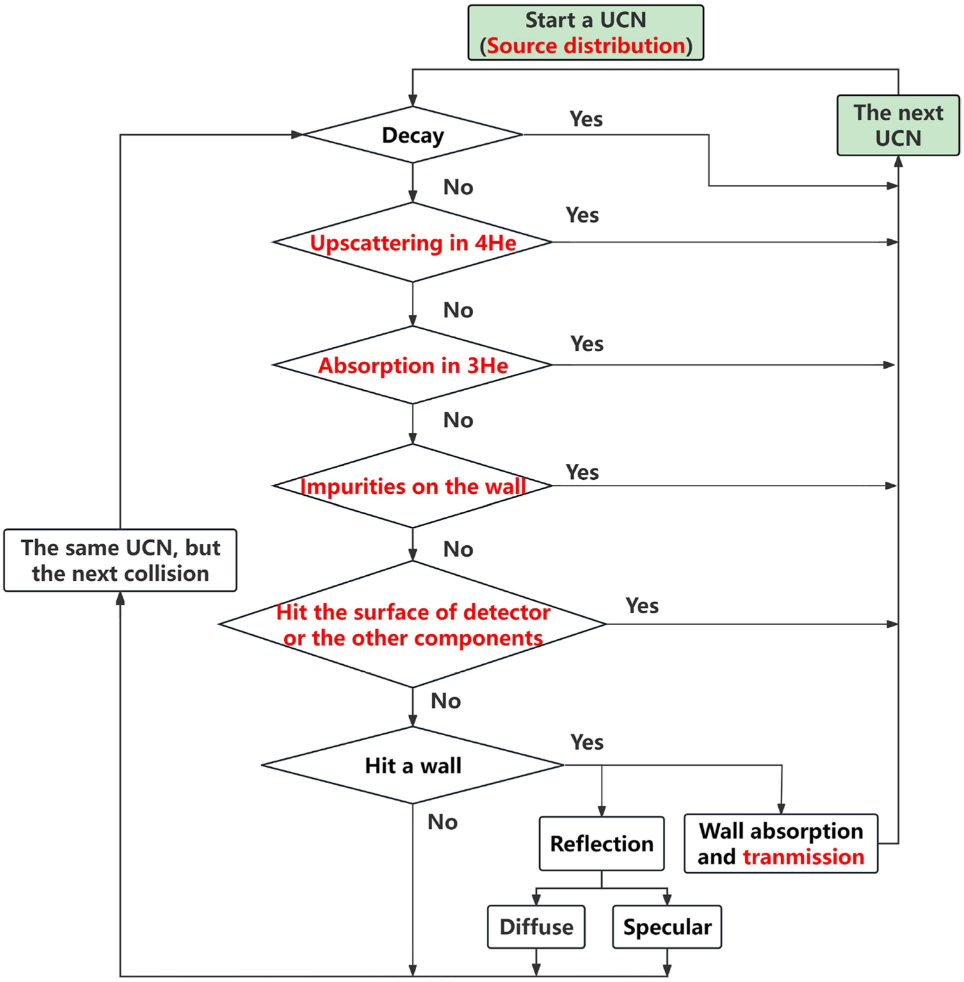

3 Comparison of the simulation by MCUCN, iMCUCN, and UCNtransport code of Lujan Center Mark3 UCN transportation system

This section elucidates the extraction efficiency comparison of the proposed Lujan Center Mark3 UCN transportation system as simulated by MCUCN, iMCUCN, and UCNtransport. A horizontal near-foil geometry is constructed, and its source and geometry are verified. The findings indicate that the variance in transmission rates simulated by UCNtransport [46] and iMCUCN is less than 10 % for the identical extraction system utilizing a He-II source at 1.6 K. The discrepancies in transmission rates simulated by MCUCN are approximately twice those obtained from UCNtransport, mainly because MCUCN lacks an upscattering physical model in SFHe.

3.1 Basic conditions

According to Ref. [45], an overview of the horizontal extraction geometry is shown in Fig. 2. 10,000 UCNs with energy below $U_{^{58}\text{Ni}} - U_{\text{He-II}} = 316.5$ neV are produced isotropically and uniformly in a 40-L He cylinder converter. As mentioned above, $\tau_{\text{up}} = 3.4$ s for 1.6 K He-II. When propagating through PP foil, the UCN transmission loss attributable to neutron elastic scattering off density inhomogeneities within the bulk is contingent upon both the macroscopic cross section and the PP foil thickness [46, 47]. With an elastic

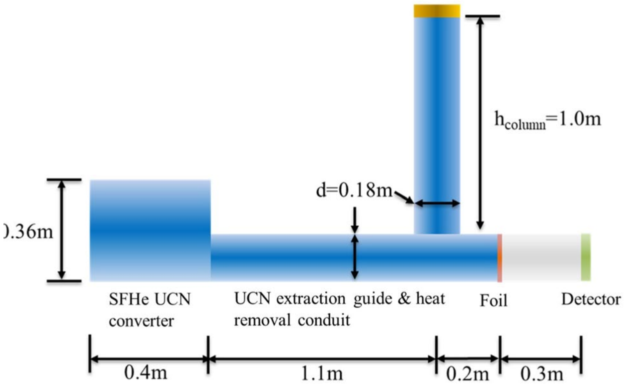

Fig. 2 (Color online) The horizontal near-foil geometry of Lujan center Mark3 UCN transportation system [45]

scattering mean-free-path, $\lambda_{\mathrm{scat}} = 20\,\mu\mathrm{m}$, for inhomogeneities, and the employed foil's thickness, $d = 30\,\mu\mathrm{m}$, the value of $\Sigma_0 \tilde{d} = 1.5$ was utilized as an input for the iMCUCN code.

The detector will count the arrival UCNs that are lower than $U_{^{58}\mathrm{Ni}}$ [45]. The input parameters in the simulation are listed in Table 1. The angular distribution for diffuse reflection follows the Lambertian model [38]. Gravity, loss due to wall absorption, upscattering effect in superfluid helium, and decay during UCN storage and transportation are included.

3.2 The energy distribution in SFHe

When UCNs are produced by inelastic scattering of 8.9 Å neutrons in superfluid helium, their angular distribution has a 6% asymmetry [48]. This real but short-lived physical process can be disregarded, so the Monte Carlo method uniformly and isotropically generates the UCNs in He-II. UCN energy distribution in He-II in iMCUCN correctly follows Eq. 8, as shown in Fig. 3. It also presents the uniform energy distribution in MCUCN.

3.3 The geometry of UCN transport system

Extending the geometry code in MCUCN to accommodate various experiments or designs is crucial. Utilizing the developed Python code, we can assess the accuracy of the constructed geometry and identify any potential gaps.

Table 1 Input parameters for the MCUCN and iMCUCN code sourced from Ref. [45]

Configuration	Parameters
Generated UCN number	10,000
Detected UCN energy	< 335 neV ($V_{^{58}\mathrm{Ni}}$)
Cylinder	$D = 0.36\,\mathrm{m}, L = 0.4\,\mathrm{m}$
Radius of guide	0.09 m
UCN Upscattering time	3.4 s (1.6 K)
UCN decay time	880 s
V_{He}	18.5 neV
$V_{^{58}\mathrm{Ni}}$	335 neV
$\eta_{^{58}\mathrm{Ni}}$	5×10^{-4}
V_{Al}	54 neV
η_{Al}	5.19×10^{-5}
Diffuse rate of Al	45%
V_{PP}	−8 neV
η_{PP}	0
λ_{scat} of idealized Al and PP	0 μm
λ_{scat} of PP	20 μm
Thickness of Al and PP	30 μm
Length of heat exchanger	1 m
Loss of foil support grid	90%
4-m guide loss to external volume	80%

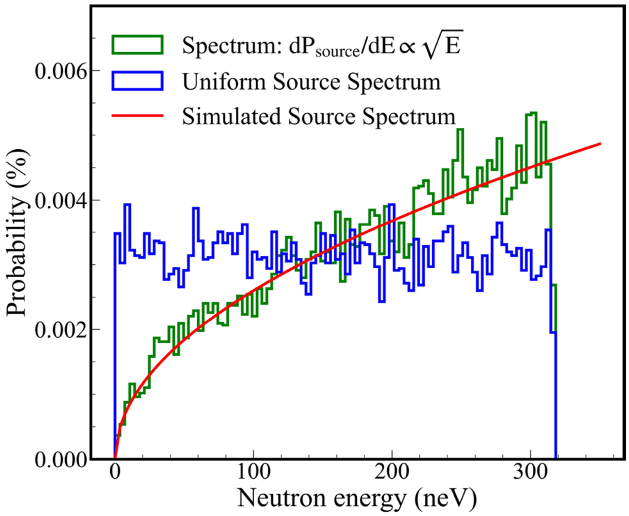

Fig. 3 (Color online) The normalized source UCN spectrum at different positions in the transport system. The red line stands for the formal expression $dP_{\mathrm{source}}/dE \propto \sqrt{E}$. The green line is the UCN spectrum distribution in the UCN converter. The blue line is the uniform UCN source distribution in MCUCN

Figure 4a, b, and c depicts the results of the simulations, indicating the points where the UCNs collide with the wall of the transport system. We projected the results into XOY, XOZ, and YOZ planes to indicate whether the geometry is the one we aim to construct and to know whether there are some gaps. Figure 4d to f provide the trajectories of UCNs on XOY, XOZ, and YOZ planes in the extraction process. The horizontal near-foil extraction geometry reveals no gaps, confirming the accuracy of the geometry model.

3.4 Comparison of the transmission rates simulated by MCUCN, iMCUCN, and UCNtransport

Tables 2 through 3 delineate the simulated outcomes by UCNtransport, MCUCN, and iMCUCN. Table 2 details the optimization process for the horizontal near-foil extraction system, changing simulation parameters based on the preceding step. A marked discrepancy in transmission rates is observed between MCUCN and UCNtransport simulations, whereas the variance between iMCUCN and UCNtransport remains under 10%. This underscores the critical role of the upscattering mechanism in iMCUCN for accurately simulating the SFHe UCN source at 1.6 K.

Furthermore, the absence of a transmission model for materials with negative optical potential in MCUCN hinders the accurate inclusion of PP foil in simulations. As per Table 2, transitioning from “switch foil from Al to ideal PP” to “Add PP elastic scattering” does not yield changes in MCUCN simulations.

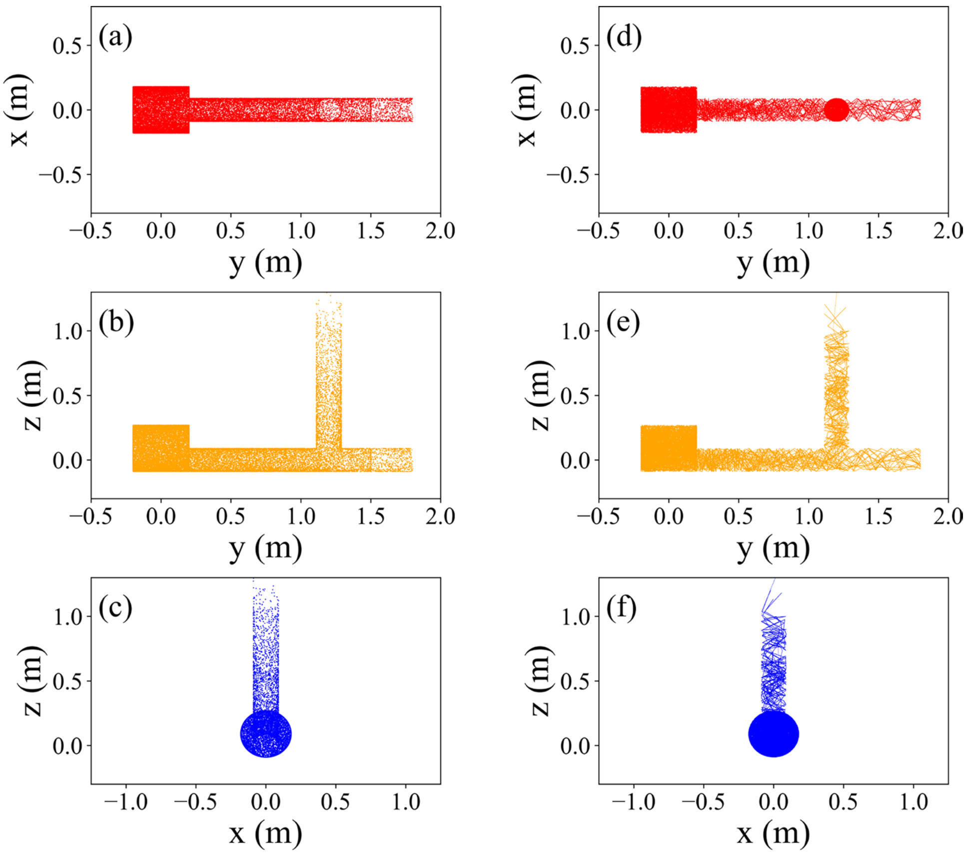

Fig. 4 (Color online) **a** to **c** show the collision points when UCNs collide with the geometry during the transport process. **d** to **f** show the trajectories of the first 100 UCNs

Table 2 Comparison of transmission rates simulated by MCUCN, iMCUCN, and UCNtransport for steps to reach $\varepsilon_{\text{sim}} = 36\%$ based on the Lujan Center Mark3 horizontal near-foil extraction system. The differences (*D*) between the simulation results of iMCUCN and UCNtransport are listed

Configuration	T_{MCUCN} (%)	T_{iMCUCN} (%)	$T_{\text{UCNtransport}}$ (%)	D (%)
Baseline: Al foil, $P_{\text{diffuse}} = 3\%$	66.6	34.1	35.0	2.6
$P_{\text{diffuse}} = 50\%$ in converter	72.6	42.1	43.0	2.1
$P_{\text{diffuse}} = 50\%$ in vertical volume	77.6	43.8	45.0	2.7
Switch foil from Al to ideal PP	85.5	49.3	53.0	7.0
Add PP elastic scattering	85.5	35.6	36.0	1.1
Add PP foil support grid loss	77.0	32.0	32.0	0.0
Add 4-m guide to external volume	61.6	25.6	26.0	1.5

Table 3 Comparison of the discrepancies between MCUCN, iMCUCN, and UCNtransport when changing the vertical column's height h_{column} with $P_{\text{diffuse}} = 50\%$ on its side walls

h_{column} (m)	T_{MCUCN} (%)	T_{iMCUCN} (%)	$T_{\text{UCNtransport}}$ (%)	D (%)
0.2	70.3	32.0	31.0	3.2
0.4	76.2	34.0	32.9	3.3
0.6	79.4	35.3	34.3	2.9
0.8	83.5	35.7	35.5	0.6
1.0	85.5	35.9	36.3	1.1
1.2	86.6	36.4	37.0	1.1

In the optimization steps detailed in Table 2, incorporating diffuse reflection within the UCN converter assists in extricating UCNs from long-lived orbits in symmetric geometries. Adding the same diffusion rate in the heat exchanger volume limits the increase in the transmission rate, as UCNs have the potential to escape from the heat exchanger. Changing Al foil to PP foil increases the rate by 8% because low-energy UCN can pass the foil. Considering the elastic scattering in the PP foil, 72% of UCNs pass through it in iMCUCN simulations, which is close to the 68% obtained by UCNtransport. "Add PP foil support grid loss" refers to the necessity of providing a support for the foil confining superfluid ^{4}He in practical applications, which results in a neutron transmission rate of 90%. The converter is located near the spallation target and requires a thick shield. Therefore, a 4-m-long UCN transport guide should be installed at the end of the system in Fig. 2, accompanied by an extraction rate of 80%.

In Table 3, the extraction rates of UCN increase with the height of the heat exchanger column when $P_{\text{diffuse}} = 50\%$

on its side walls. The results simulated by MCUCN are more than two times those simulated by iMCUCN. However, the differences between iMCUCN and UCNtransport at various column heights are less than 10%.

In conclusion, the simulation results from iMCUCN and UCNtransport are in agreement.

4 Comparison of MCUCN, iMCUCN simulated, and SUN1 experimental results

To confirm the validity of the iMCUCN code, we perform simulation by MCUCN and iMCUCN and compared the result with the SUN1 measured results reported by Oliver Zimmer et al. [39, 49]. The analysis revealed that the disparities in count rates between the experimental measurements and iMCUCN simulations are small. In contrast, the predicted transmission rates by MCUCN exhibit deviations from the experimental results. This discrepancy predominantly arises from the lack of essential physical processes in MCUCN.

4.1 The experimental configuration and parameters

Figure 5 illustrates the experimental configuration. The ^{4}He converter exhibits a rectangular geometry measuring 100 cm × 7 cm × 7 cm, with Be coated on the front and rear faces and BeO used for the sides. The vertically oriented extraction guide is positioned at a height of 10 cm, with the shutter situated midway along its length. Following this, there is a 7-cm horizontal bend leading to a second vertical guide extending for 15 cm, ultimately leading to the detector at its end. Constructed from stainless steel, the guides have a diameter of 23 mm. The gap area at the shutter is 1.73 mm^2.

Table 4 Input parameters for the SUN1 experiment utilized in the simulation [39, 49]

Configuration	Parameters
Converter dimensions	100 cm × 7 cm × 7 cm
Radius of guide	0.0115 m
V_{He}	18.5 neV
V_{BeO}	261.0 neV
η_{BeO}	1.35×10^{-5}
V_{Be}	252.0 neV
η_{Be}	5×10^{-6}
$V_{\mathrm{stainless}}$	183.0 neV
$\eta_{\mathrm{stainless}}$	9.3×10^{-5}
Open shutter at	804 s
Close shutter at	937 s

Refer to Table 4 for detailed information on various input parameters.

The initial UCN spectrum follows Eq. 8, and the maximum energy is 261 neV decided by the optical potential of BeO. The measured UCN count rate at the detector of the SUN1 system is depicted in Fig. 6. During a scenario where cold neutrons are incident, while the shutter is closed, the detector detects UCNs, attributed to small gap between shutter and guide. The UCN count rates at the detector reached a saturation point after approximately 200 s. At around 800 s, the cold neutron beam was deactivated, coinciding with the shutter's opening to the UCN guide. A peak in the UCN count rate at the detector was observed after about 3 s. Subsequently, the shutter was closed after 135 s.

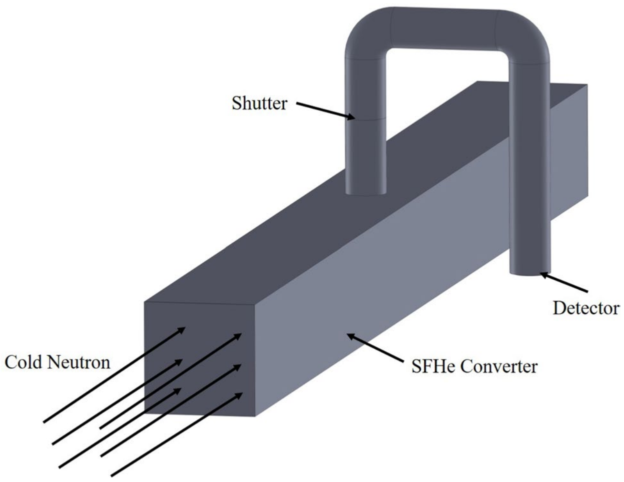

Fig. 5 The geometry of SUN1 [39, 49]

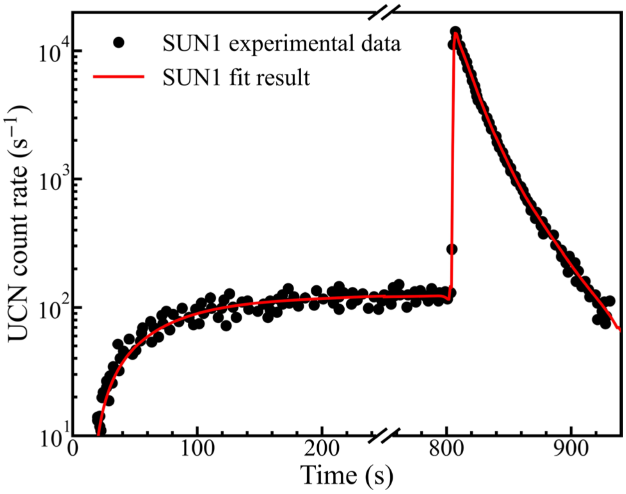

Fig. 6 (Color online) SUN1 experimental results at detector. The red lines are fitted [39, 49]

4.2 Scenario before opening shutter

Before opening the shutter, the UCN number in the converter as a function of time is [38]:

$$N(t) = \rho(t)V = VP\tau\left(1 - \mathrm{e}^{-\frac{t}{\tau}}\right), \tag{9}$$

where $\rho(t)$ is the UCN density in the converter. V is the volume of the converter. P is the UCN production rate per unit volume. τ is the buildup time, as defined in Eq. (1), representing the UCN surviving time in the SFHe converter. The UCN number can reach a saturation point when the UCN generated time is sufficiently long, and the saturation UCN number in the UCN converter will be

$$N_{\mathrm{sat}} = VP\tau, \tag{10}$$

where N_{sat} represents the saturation UCN number in the converter .

The UCN count rate at the detector in Fig. 6 can be expressed as

$$C(t) \propto N(t)\frac{1}{\tau_{\mathrm{gap}}}, \tag{11}$$

τ_{gap} is determined by the gap area between the shutter and the guide before the shutter is opened. It also follows Eq. (5).

In the converter, the β decay term remains constant, and the absorption of ^{3}He is not disregarded under this condition. Both the He-II upscattering and the abundance of ^{3}He are independent of UCN velocity. According to Ref. [39], it was reported that $\tau^{-1}_{\mathrm{experiment}} = (67\,\mathrm{s})^{-1}$, $\tau^{-1}_{\mathrm{abs}} = (315\,\mathrm{s})^{-1}$, $\tau^{-1}_{\beta} = (880\,\mathrm{s})^{-1}$, $\tau^{-1}_{\mathrm{up}} = (1247\,\mathrm{s})^{-1}$, $\tau^{-1}_{\mathrm{wall}} = (278\,\mathrm{s})^{-1}$. Therefore, $\tau^{-1}_{\mathrm{leakage}} + \tau^{-1}_{\mathrm{impurities}} = (161\,\mathrm{s})^{-1}$. Both the impurities time constant and leakage time constant remain ambiguous. To simplify the simulation, we assume that the losses caused by impurities and leakage are energy-dependent, similar to wall loss.

The leakage count rate at the detector is proportional to the area of the gap between the shutter and guide. The gap of the shutter, unspecified in Ref. [39, 49], can only be determined by comparing with simulated results through changing the size of gap. As illustrated in Fig. 7, we observed an increase in the UCN count rate before opening the shutter with increasing shutter gap size because the leakage rate is proportional to the gap area. The gap whose simulation results coincide with the experimental results before opening the shutter is determined to be 1.73 mm^2.

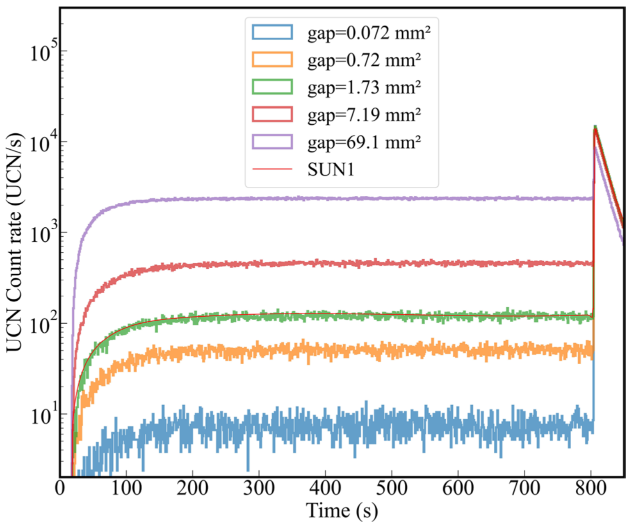

Fig. 7 (Color online) Fit the shutter gap

4.3 Scenario after opening of the shutter

After opening the shutter, the accumulated UCNs in the converter will be released. Neglecting gravity and the energy distribution of UCNs, and closing the shutter of cold neutron, the decay of UCNs in the converter after opening the shutter can be

$$N(t) = N_{\mathrm{sat}}\mathrm{e}^{-t\left(\frac{1}{\tau_{\mathrm{guide}}} + \frac{1}{\tau}\right)}, \tag{12}$$

where τ_{guide} is the guide leakage constant after opening the shutter. According to Eq. 11, the UCN count rate at the detector can be expressed as $C(t) \propto N(t)\frac{1}{\tau_{\mathrm{guide}}}$. In real scenarios, this process is dependent on the UCN energy in the converter. Thus the UCN number in the converter does not follow a strict one time constant decay. The UCN count rate at the detector before opening the shutter is nearly proportional to UCN total number in the converter, and researchers [39, 49] utilize two time decay constants to fit the detected UCN count rate after opening the shutter. In the SUN1 experiment, the fitted two decay time constants are (13 ± 1) s and (34 ± 1) s.

The decay time after opening the shutter is primarily influenced by the area of the guide, which has been determined experimentally. It can also be affected by the unknown diffuse reflection probabilities of the guide (d_{g}) and converter (d_{c}). The diffuse reflection probability of polished stainless steel coated in the guide typically falls within the range of 1% to 3%. Therefore, we present the decay time constants for some results in Table 5.

The optimal condition corresponds to a converter diffuse reflection probability $d_{\mathrm{c}} = 3.0\%$, a guide diffuse

Table 5 The two decay time constants under different conditions

	d_g (%)	d_c (%)	τ (s)	τ_1 (s)	τ_2 (s)
SUN1 in [39]	–	–	67	13	34
iMCUCN	0.5	3.0	73.4	12.6	30.3
	1.5	3.0	71.0	13.7	31.7
	5.0	3.0	83.3	16.1	35.1
	8.0	3.0	82.6	17.5	35.1
	10.0	3.0	80.9	19.4	42.0
iMCUCN	1.5	1.0	78.4	13.9	32.8
	1.5	3.0	71.0	13.7	31.7
	1.5	5.0	77.9	11.9	26.4
	1.5	10.0	83.2	14.0	31.8

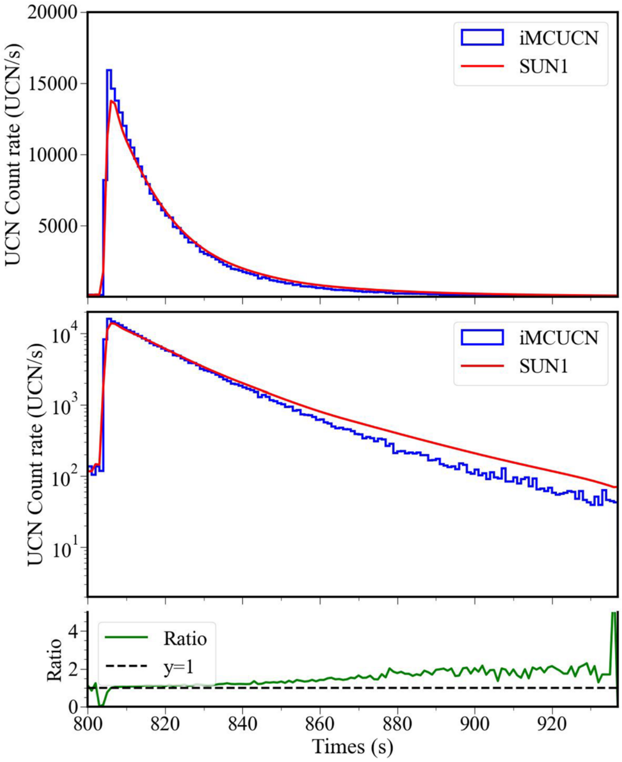

Fig. 8 (Color online) The top figure compares the simulation results of the iMCUCN with the measured data under the selected conditions. The middle figure is identical to the top figure, but is presented in logarithmic coordinates. The figure illustrates the ratio of the experimental data to the iMCUCN simulation data

reflection probability $d_g = 1.5\%$. The final buildup time is 71.0 s, and the two decay time constants are 13.7 s and 31.7 s. And the comparison between the simulated results and the measured results under this condition is shown in Fig. 8. The simulation results from iMCUCN under this condition closely align with the experimental data. Specifically, UCNs with lower energy contribute to the second decay time constant τ_2. The discrepancy ranging from 840 s to 937 s between SUN1 measurements and data simulated by iMCUCN may arise from several factors. Firstly, the UCN spectrum generated in simulation may differ from the actual conditions in the experiment. Secondly, errors may be presented in the data reading process from [39]. To clarify these discrepancies, further experiments need to be conducted.

4.4 Discussion

To further enhance comprehension of the underlying physics discussed in this section, additional details will be presented below.

The results obtained with $d_c = 3.0\%$ and $d_g = 1.5\%$ as simulated by MCUCN exhibit discrepancies with the experimental data depicted in the upper panel of Fig. 9. In the MCUCN simulation, the buildup time is 153.0 s, and the decay time constants are 15.3 s and 38.3 s. In the absence of losses due to impurities, leakage, absorption of ^{3}He, and upscattering in ^{4}He, the time required to reach the saturation UCN count rate is longer, allowing more UCNs to survive and be extracted. According to Eq. 3, wall loss depends on UCN energy, i.e., the lower the UCN energy, the smaller the chance of being lost after collision with the wall. The velocity of low-energy UCN is slower and takes more time to reach the detector. Therefore, the slope of the UCN count rate at detector after opening shutter simulated by MCUCN is relatively smaller than that simulated by iMCUCN in the upper panel of Fig. 9.

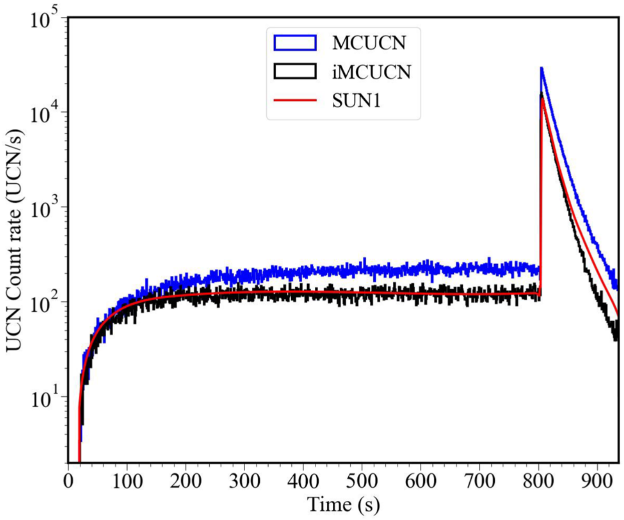

Fig. 9 (Color online) The figure compares the simulation results of the iMCUCN and MCUCN with the measured data under the optimal condition. The data simulated by the iMCUCN agree with the measured data, while that of MCUCN show discrepancies

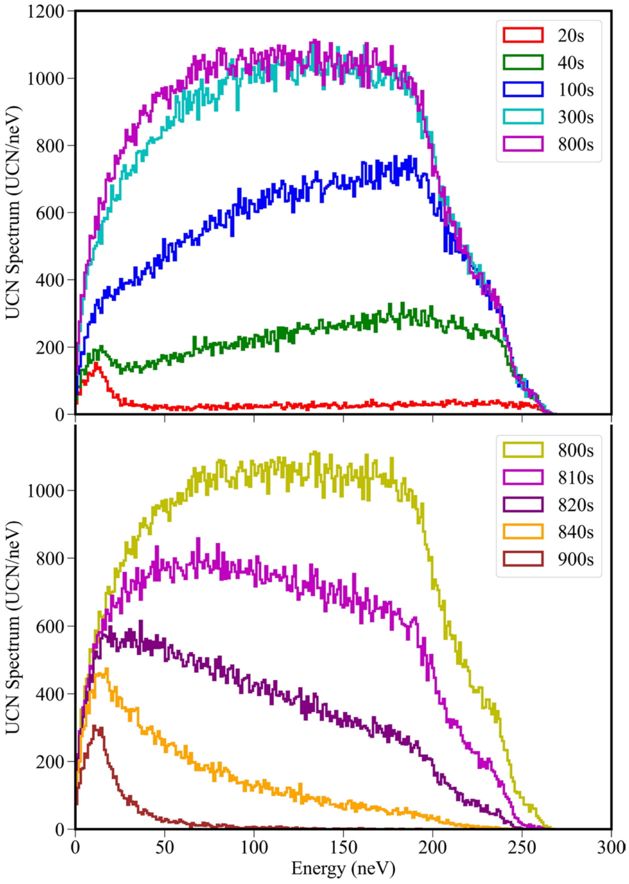

Fig. 10 (Color online) The top figure illustrates the UCN spectrum in the converter simulated by iMCUCN before 800 s, showing the change over time. The bottom figure represents the spectrum after 800 s

Figure 10 depicts the UCN spectrum within the converter at various time points simulated by iMCUCN. The figure at the top shows the UCN spectrum in the converter simulated by iMCUCN before 800 s, depicting the change over time. Initially, at 20 s, the UCNs begin to accumulate within the converter. Approximately 300 s later, a saturation point is nearly reached, indicating that the rate of UCN accumulation has equalized with the rate of their loss. However, from 804 s, the UCN spectrum within the converter begins to decrease due to the opening of the shutter. It is noteworthy that the saturated UCN spectrum observed at 800 s does not strictly adhere to the expected distribution as described by Eq. 8. This deviation is attributed to the presence of energy-dependent loss mechanisms, including impurities, leakage, and interactions with the converter walls. The figure below displays the UCN spectrum in the converter simulated by iMCUCN after 800 s. At 810 s, a greater number of faster UCNs have been extracted compared to those with lower energy. By 900 s, the majority of the UCN have been extracted, with only a small number of low-energy UCN

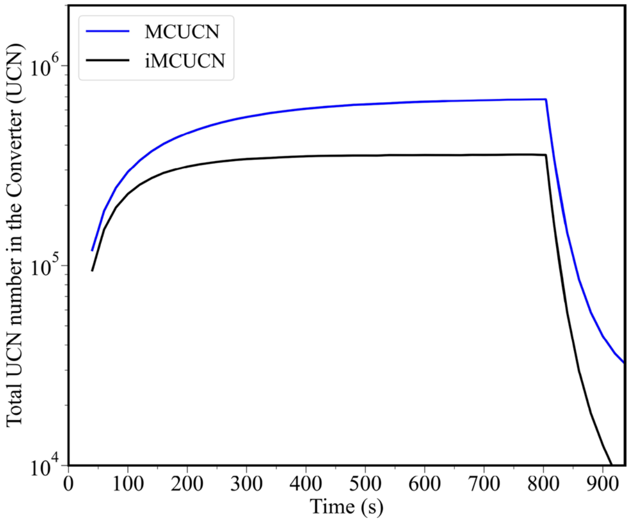

Fig. 11 (Color online) The total UCN number in the converter as a function of time simulated by iMCUCN and MCUCN

remaining in the converter. The optical potentials of BeO, Be, and stainless steel are 261 neV, 252 neV, and 183 neV, respectively. UCNs with energy lower than 183 neV can be more effectively constrained than those ranging from 183 neV to 252 neV, as some of them may escape from the stainless steel guide before the shutter. UCNs with energies between 252 neV and 261 neV will be less constrained due to the presence of Be surfaces.

The total UCN number within the converter can be illustrated through simulation, as visualized in Fig. 11. Notably, there exists a significant discrepancy between the MCUCN simulated total UCN number and those obtained from the iMCUCN simulation within the converter due to the lack of

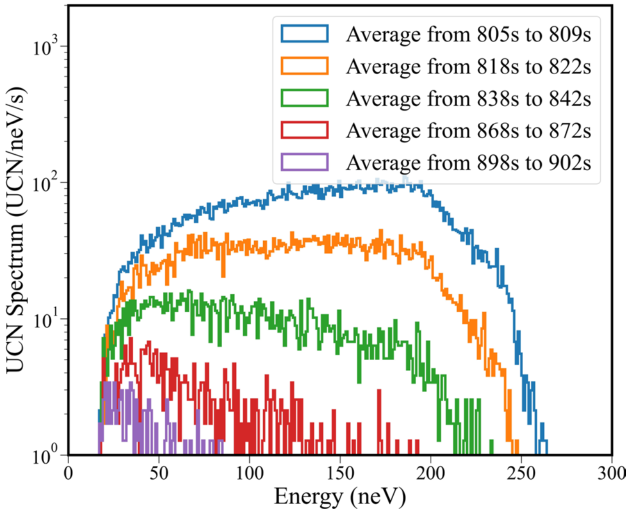

Fig. 12 (Color online) The detected UCN spectrum at detector with a function of time

losses models of impurities, leakage, absorption of ^{3}He, and upscattering in ^{4}He in MCUCN.

Figure 12 illustrates the UCN spectrum at the detector. Prior to the opening of the shutter, the spectrum at the detector remains low due to the small leakage rate from the gap and the low statistical UCN count rate. At about 807 s, the UCN spectrum is near to the peak, indicating a significant extraction of UCNs to the detector. Higher energy UCNs dominate the spectrum during this period. Subsequently, after 33 s, the extracted UCN number notably decreases, with lower energy UCNs becoming more prominent than higher energy ones. At 870 s, only lower energy UCNs remain. Finally, by 900 s, only a few lower energy UCNs can be extracted and detected at the detector.

5 Conclusion

In this paper, we extended the capabilities of the MCUCN code by incorporating the upscattering effect of ^{4}He, absorption of ^{3}He in superfluid helium, upscattering and absorption of impurities, source energy distribution in SFHe, and a transmission model for materials with negative optical potential, as well as geometry description. We thoroughly validated the source and geometry parameters. Subsequent analysis showed that the data simulated by iMCUCN were in close agreement with the simulations conducted by UCNtransport for the Lujan Center Mark3 UCN transport system and the SUN1 experimental data. These results demonstrate that iMCUCN is effective for simulating UCN storage and transport in SFHe UCN sources.

Acknowledgements The authors would like to thank Dr. Zsigmond Geza for help in understanding the details of the original MCUCN code and Prof. Kent Leung for help in understanding the origin of the elastic scattering in the inhomogeneous foil.

Author contributions Xue-Fen Han, Tian-Jiao Liang, and Robert Golub contributed to the study conception and design. Material preparation, data collection, and analysis were performed by Xue-Fen Han. The first draft of the manuscript was written by Xue-Fen Han, and all authors commented on previous versions of the manuscript. All authors read and approved the final manuscript.

Data availability The data that support the findings of this study are openly available in Science Data Bank at https://cstr.cn/31253.11.sciencedb.j00186.00852 and https://www.doi.org/10.57760/sciencedb.j00186.00852.

Declarations

Conflict of interest The authors declare that they have no competing interests.

References

1. K. Kirch, B. Lauss, P. Schmidt-Wellenburg et al., Ultracold neutrons-physics and production. Nucl. Phys. News **20**, 17–23 (2010). https://doi.org/10.1080/10619121003626724
2. E. Fermi, W.H. Zinn, Reflection of neutrons on mirrors. Paper presented at International Conference on Fundamental Particles and Low Temperatures (1947), Cambridge, UK, 22–27 July 1946. https://books.google.de/books?id=IKsY9gzauzUC
3. E. Fermi, L. Marshall, Interference phenomena of slow neutrons. Phys. Rev. **71**, 666 (1947). https://doi.org/10.1103/PhysRev.71.666
4. V.I. Lushchikov, Y.N. Pokotilovskii, A.V. Strelkov et al., Observation of ultracold neutrons. JETP Lett. **9**, 40–45 (1969)
5. A. Steyerl, Measurements of total cross sections for very slow neutrons with velocities from 100 m/sec to 5 m/sec. Phys. Rev. B **29**, 33–35 (1969). https://doi.org/10.1016/0370-2693(69)90127-0
6. C. Abel, S. Afach, N.J. Ayres, Measurement of the permanent electric dipole moment of the neutron. Phys. Rev. Lett. **124**, 081803 (2020). https://doi.org/10.1103/PhysRevLett.124.081803
7. F.M. Gonzalez, E.M. Fries, C. Cude-Woods et al., Improved neutron lifetime measurement with UCNτ. Phys. Rev. Lett. **127**, 162501 (2021). https://doi.org/10.1103/PhysRevLett.127.162501
8. M.A.-P. Brown, E.B. Dees, E. Adamek, New result for the neutron β-asymmetry parameter A_0 from UCNA. Phys. Rev. C **97**, 035505 (2018). https://doi.org/10.1103/PhysRevC.97.035505
9. X. Sun, E. Adamek, B. Allgeier et al., Improved limits on Fierz interference using asymmetry measurements from the Ultracold Neutron Asymmetry (UCNA) experiment. Phys. Rev. C **101**, 035503 (2020). https://doi.org/10.1103/PhysRevC.101.035503
10. R. Sedmik, J. Bosina, L. Achatz, Proof of principle for Ramsey-type gravity resonance spectroscopy with qBounce. EPJ Web Conf. **219**, 05004 (2019). https://doi.org/10.1051/epjconf/201921905004
11. T. Jenke, H. Abele, Experiments with gravitationally-bound ultracold neutrons at the European Spallation Source ESS. Phys. Procedia **51**, 67–72 (2014). https://doi.org/10.1016/j.phpro.2013.12.016
12. L. Broussard, Ultracold neutron physics at the Los Alamos National Laboratory. In *20th International Conference on Particles and Nuclei*, 444–447 (2014). https://doi.org/10.3204/DESY-PROC-2014-04/116
13. W.M. Snow, Toward an improved search for neutron–antineutron oscillations. Nucl. Instrum. Methods A **611**, 144–148 (2009). https://doi.org/10.1016/j.nima.2009.07.049
14. S. Arzumanov, L. Bondarenko, P. Geltenbort et al., Investigation of the radiative capture of UCN at the matter surface. Nucl. Instrum. Methods A **440**, 690–694 (2000). https://doi.org/10.1016/S0168-9002(99)01063-3
15. A.D. Sakharov, Violation of CP invariance, C asymmetry, and baryon asymmetry of the universe. Sov. Phys. Usp. **34**, 392 (1991). https://doi.org/10.1070/PU1991v034n05ABEH002497
16. C.Y. Liu, Ph.D. thesis, Princeton University (2002)
17. H.M. Shimizu, Y. Iwashita, M. Kitaguchi et al., A transport optics for pulsed ultracold neutron sources. Nucl. Instrum. Methods A **634**, 25–27 (2011). https://doi.org/10.1016/j.nima.2010.06.210
18. I. Altarev, Y.V. Borisov, A.B. Brandin et al., A liquid hydrogen source of ultra-cold neutrons. Phys. Lett. A **80**, 413–416 (1980). https://doi.org/10.1016/0375-9601(80)90784-7
19. A. Serebrov, V. Mityukhlyaev, A. Zakharov et al., Experimental study of a solid-deuterium source of ultracold neutrons. JETP Lett. **62**, 785–790 (1995)
20. A. Serebrov, V. Mityukhlyaev, A. Zakharov, Studies of a solid-deuterium source for ultra-cold neutrons. Nucl. Instrum. Methods

A **440**, 658–665 (2000). https://doi.org/10.1016/S0168-9002(99)01058-X
21. A.P. Serebrov, V.A. Mityukhlyaev, A.A. Zakharov et al., Solid deuterium source of ultracold neutrons based on a pulsed spallation source. JETP Lett. **66**, 802–808 (1997). https://doi.org/10.1134/1.567601
22. A.P. Serebrov, Solid deuterium and UCN factory: application to the neutron electric dipole moment measurement. Nucl. Instrum. Methods A **440**, 653–657 (2000). https://doi.org/10.1016/S0168-9002(99)01057-8
23. A. Saunders, J.M. Anaya, T.J. Bowles et al., Demonstration of a solid deuterium source of ultra-cold neutrons. Phys. Rev. B **593**, 55–60 (2004). https://doi.org/10.1016/j.physletb.2004.04.048
24. M. Daum, UCN collaboration, an ultracold neutron facility at PSI. AIP Conf. Proc. **549**, 888–889 (2000). https://doi.org/10.1063/1.1345387
25. A. Frei, Y. Sobolev, I. Altarev et al., First production of ultracold neutrons with a solid deuterium source at the pulsed reactor TRIGA Mainz. Eur. Phys. J. A **34**, 119–127 (2007). https://doi.org/10.1140/epja/i2007-10494-2
26. G. Bison, M. Daum, K. Kirch et al., Comparison of ultracold neutron sources for fundamental physics measurements. Phys. Rev. C **95**, 045503 (2017). https://doi.org/10.1103/PhysRevC.95.045503
27. T.M. Ito, E.R. Adamek, N.B. Callahan et al., Performance of the upgraded ultracold neutron source at Los Alamos National Laboratory and its implication for a possible neutron electric dipole moment experiment. Phys. Rev. C **97**, 012501 (2018). https://doi.org/10.1103/PhysRevC.97.012501
28. J. Wu, X. Li, B. Wu et al., Design and commissioning of a wideband RF system for CSNS-II rapid-cycling synchrotron. Nucl. Sci. Tech. **35**, 5 (2024). https://doi.org/10.1007/s41365-024-01377-6
29. S.D. Tang, Y.H. Chen, J.Y. Tang et al., Nondestructive technique for identifying nuclides using neutron resonance transmission analysis at CSNS Back-n. Nucl. Sci. Tech. **35**, 17 (2024). https://doi.org/10.1007/s41365-024-01367-8
30. H. Liu, S. Wang, Longitudinal beam dynamic design of 500kW beam power upgrade for CSNS-II RCS. Radiat. Detect. Technol. Methods **6**, 339–348 (2022). https://doi.org/10.1007/s41605-022-00325-5
31. Y. Hong, Y.P. Song, L.P. Zhou et al., Beamline design for multipurpose muon beams at CSNS EMuS. Nucl. Sci. Tech. **35**, 38 (2024). https://doi.org/10.1007/s41365-024-01406-4
32. B. Wu, X. Li, Z. Li et al., Development of a large nanocrystalline soft magnetic alloy core with high $\mu_p'Qf$ products for CSNS-II. Nucl. Sci. Tech. **33**, 99 (2022). https://doi.org/10.1007/s41365-022-01087-x
33. W. Schreyer, T. Kikawa, M.J. Losekamm et al., PENTrack—a simulation tool for ultracold neutrons, protons, and electrons in complex electromagnetic fields and geometries. Nucl. Instrum. Methods A **858**, 123–129 (2017). https://doi.org/10.1016/j.nima.2017.03.036
34. F. Atchison, T. Brys, M. Daum et al., The simulation of ultracold neutron experiments using GEANT4. Nucl. Instrum. Methods A **552**, 513–521 (2005). https://doi.org/10.1016/j.nima.2005.06.065
35. A.T. Holley, Ph.D. thesis, North Carolina State University (2012)
36. G. Zsigmond, The MCUCN simulation code for ultracold neutron physics. Nucl. Instrum. Methods A **881**, 16–26 (2018). https://doi.org/10.1016/j.nima.2017.10.065
37. R. Golub, J.M. Pendlebury, The interaction of Ultra-Cold Neutrons (UCN) with liquid helium and a superthermal UCN source. Phys. Lett. A **62**, 337–339 (1977). https://doi.org/10.1016/0375-9601(77)90434-0
38. R. Golub, D. Richardson, S.K. Lamoreaux, *Ultra-cold neutrons* (Taylor & Francis, New York, 1991), pp. 62–104
39. F.M. Piegsa, M. Fertl, S.N. Ivanov et al., New source for ultracold neutrons at the Institut Laue-Langevin. Phys. Rev. C **90**, 015501 (2014). https://doi.org/10.1103/PhysRevC.90.015501
40. R. Golub, On the storage of neutrons in superfluid ^{4}He. Phys. Rev. A **72**, 387–390 (1979). https://doi.org/10.1016/0375-9601(79)90505-X
41. H. Yoshiki, K. Sakai, M. Ogura et al., Observation of ultracold-neutron production by 9-Å cold neutrons in superfluid helium. Phys. Rev. Lett. **68**, 1323–1326 (1992). https://doi.org/10.1103/PhysRevLett.68.1323
42. K.K.H. Leung, S. Ivanov, F.M. Piegsa et al., Ultracold-neutron production and up-scattering in superfluid helium between 1.1 K and 2.4 K. Phys. Rev. C **93**, 025501 (2016). https://doi.org/10.1103/PhysRevC.93.025501
43. R. Golub, S.K. Lamoreaux, Production and storage of ultracold neutrons in superfluid ^{4}He. Phys. Rev. Lett. **70**, 517 (1993). https://doi.org/10.1103/PhysRevLett.70.517
44. R. Golub, C. Jewell, P. Ageron et al., Operation of a superthermal ultra-cold neutron source and the storage of ultra-cold neutrons in superfluid helium^4. Z. Phys. B Con. Mat. **51**, 187–193 (1983). https://doi.org/10.1007/BF01307673
45. K.K.H. Leung, G. Muhrer, T. Hugle, A next-generation inverse-geometry spallation-driven ultracold neutron source. J. Appl. Phys. **126**, 224901 (2019). https://doi.org/10.1063/1.5109879
46. Y.N. Pokotilovski, Effect of oxide films and structural inhomogeneities on transmission of ultracold neutrons through foils. Eur. Phys. J. Appl. Phys. **73**, 20302 (2016). https://doi.org/10.1051/epjap/2016150073
47. P.C. Miranda, Ultra-cold neutron transmission of clear and metal-coated polypropylene windows. J. Phys. D Appl. Phys. **21**, 1326 (1988). https://doi.org/10.1088/0022-3727/21/9/003
48. S.K. Lamoreaux, R. Golub, The angular distribution of ultracold neutrons produced by scattering cold neutrons in superfluid ^{4}He. Pis'ma ZhETF **58**, 844–846 (1993)
49. O. Zimmer, F.M. Piegsa, S.N. Ivanov et al., Superthermal source of ultracold neutrons for fundamental physics experiments. Phys. Rev. Lett. **107**, 134801 (2011). https://doi.org/10.1103/PhysRevLett.107.134801

Springer Nature or its licensor (e.g. a society or other partner) holds exclusive rights to this article under a publishing agreement with the author(s) or other rightsholder(s); author self-archiving of the accepted manuscript version of this article is solely governed by the terms of such publishing agreement and applicable law.